Research Article Vol. 38, No. 12 / December 2021 / Journal of the Optical Society of America A 1853

Journal of the Optical Society of America A

OPTICS, IMAGE SCIENCE, AND VISION

Measurement of chromatic aberrations using phase retrieval

Matthew D. Bergkoetter,[1,2] Brian E. Kruschwitz,[3] Seung-Whan Bahk,[3] and James R. Fienup[1,*]

[1]The Institute of Optics, University of Rochester, Rochester, New York 14627, USA
[2]NASA Goddard Space Flight Center, Greenbelt, Maryland 20771, USA
[3]Laboratory for Laser Energetics, University of Rochester, 250 East River Road, New York 14623-1299, USA
*Corresponding author: fienup@optics.rochester.edu

Received 5 July 2021; revised 4 October 2021; accepted 4 October 2021; posted 7 October 2021 (Doc. ID 431117); published 24 November 2021

We explore the feasibility of measuring chromatic aberrations using a technique based on phase retrieval, primarily for the purpose of diagnostics on the OMEGA EP laser. A computational model and optimization strategy are described, issues of numerical efficiency are addressed, and the potential limitations of the method are studied using mathematical analysis and Monte Carlo simulations. The algorithm performs well in simulation and yields encouraging results in a small-scale laboratory experiment.

https://doi.org/10.1364/JOSAA.431117

1. INTRODUCTION

Phase retrieval is a computational method for estimating the phase of an electromagnetic field based on measurements of the intensity in one or more planes. For wavefront-sensing applications, the phase of interest is in the pupil plane of an optical system, and typically the aperture and image-plane intensity are known [1,2]. The image-plane intensity is often an image of a single point source, known as the point spread function (PSF). The iterative process of retrieving the phase involves forming an initial estimate of the wavefront in the pupil plane, simulating a propagation of that field to the image plane (which typically involves a Fourier transform), and comparing the resulting intensity distribution with the measured intensity via an error metric. The wavefront estimate is then modified to improve agreement in the image plane, based on a calculation of the gradient (and possibly the second-order derivative) of the error metric with respect to wavefront parameters. A wide variety of strategies to improve the wavefront estimate exists, and may generally be understood in the broader mathematical context of nonlinear optimization [3–5].

Among the various applications of this general approach is the improvement of diagnostic tools for the OMEGA EP laser [6,7]. In this case, phase retrieval complements measurements provided by a conventional Shack–Hartmann wavefront sensor (SHWFS) with an estimate of non-common path error, and of differential pistons between regions of the segmented beam [8,9]. A proposed way to improve this system is to also estimate for chromatic aberrations in the system. These can arise in a chirped-pulse amplification (CPA) laser such as OMEGA EP in the form of residual angular dispersion from the pulse stretcher and compressor, which significantly degrade focal-spot quality [10,11]. They can also arise in the form of axial dispersion (also called axial color or longitudinal chromatic aberration) due to transmissive elements [12]. These, if uncompensated for, can lead to significant reduction of the focused intensity for a large beam or a short (femtosecond) pulse. This effect increases more for multi-pass lens-based image-relayed amplifiers. A special compensator was installed for the Multi-Terawatt Optical Parametric Amplification Line (MTW-OPAL) laser (20 fs) at the Laboratory for Laser Energetics, without which the intensity would have been reduced more than five times [13]. Even for picosecond pulses, this effect can be nonnegligible. A detailed beam propagation simulation for the Advanced Radiographic Capability (ARC) laser system at the National Ignition Facility (NIF) estimates a 30% reduction in intensity [14].

In this paper, we will explore the feasibility of joint retrieval of angular dispersion, axial dispersion, and monochromatic aberrations through simulations, theoretical analysis, and a laboratory demonstration.

2. SIMULATION MODEL

A. Modal Chromatic Aberrations

A general way to model chromatic aberration would be to allow the wavefront estimate for each spectral component to vary independently of the others, and this has been shown to be effective in phase-retrieval simulations [15] with a small number of discrete wavelengths. However, the work reported in [15] retrieved wavefronts for five discrete spectral components distributed over a bandwidth of 176 nm, which is much larger than

the bandwidths typically seen on OMEGA EP, such as 3.5 nm for fully amplified compressed pulses and 8 nm for unamplified test shots. For a coarse spectral sampling, the dependency of Fraunhofer diffraction on wavelength alone has significant effects, i.e., a wavefront estimate for one spectral component produces a noticeably different PSF than if the same wavefront was applied to another spectral component. The distinct effects of applying a wavefront estimate to a particular spectral component means that the particular distribution of wavefronts over the spectrum that produces the correct broadband PSF is relatively unambiguous. For a model with denser spectral sampling, on the other hand, the effects of applying the same wavefront modification to different spectral components are more similar to one another, which makes the correct distribution of wavefronts across the spectrum harder to determine. In this case, we can instead use a modal approach to modeling chromatic effects, and require that the wavefronts estimated for the various spectral components be related in a physically meaningful way. For example, the simplest form of angular dispersion can be modeled as a wavefront tilt that varies linearly with wavelength. Similarly, first-order longitudinal chromatic aberration is a defocus that varies linearly with wavelength. By forcing the spectrally varying components of the wavefronts to fit this model, we can mitigate uniqueness problems that would arise if they were allowed to vary independently. This approach has the added benefit of reducing the dimensionality of the parameter space that must be searched to find the optimal phase estimate, which generally reduces time to convergence. This does come at the expense of reducing the scope of the chromatic effects that can be modeled, but the modal approach can be extended to include higher-order effects, or instead may be followed up by another round of optimization with another more-detailed model as part of a bootstrapping process. In the present work, a linear model was adequate to fit the data.

In our model, we will assume that there is an initial estimate of the monochromatic wavefront W_0 measured by a SHWFS, and that there is also non-common path error between the SHWFS and the focusing optics that must be estimated in terms of a monochromatic wavefront W_M, in addition to the chromatic aberrations $(\lambda - \lambda_r)\, W_C$, so that

$$W(\xi, \eta; \lambda) = W_0(\xi, \eta) + W_M(\xi, \eta) + (\lambda - \lambda_r)\; W_C(\xi, \eta), \tag{1a}$$

$$W_M(\xi, \eta) \equiv \sum_{n=0}^{N} a_n Z_n(\xi, \eta), \tag{1b}$$

$$W_C(\xi, \eta) \equiv \sum_{n=0}^{N_c} c_n Z_n(\xi, \eta), \tag{1c}$$

where ξ and η are pupil-plane coordinates, λ is the wavelength of a single spectral component, and Z_n is the nth Zernike polynomial. The monochromatic wavefront at a reference wavelength λ_r (which we will nominally take to be the center of the spectrum) is the sum of the known component W_0, and the unknown wavefront W_M, while chromatic effects are accounted for by the second sum with coefficients c_n, which modify the reference wavefront for each spectral component.

The phase retrieval algorithm will jointly estimate the unknown monochromatic wavefront along with the chromatic aberrations in terms of the sets of coefficients a_n and c_n, respectively. The exit pupil amplitude is assumed to be a known aperture with transmittance $P(\xi, \eta)$, and each spectral component has a scalar amplitude weight of A_k. For this work, we assume that A_k captures the only dependence of the pupil amplitude on wavelength, i.e., that $P(\xi, \eta)$ is the same for every spectral component. Each spectral component is propagated from the pupil plane to the image plane separately, so if there are K total spectral components, the kth field is

$$g_k(\xi, \eta) = A_k P(\xi, \eta) \exp\left[\frac{i2\pi}{\lambda_k} W(\xi, \eta; \lambda_k)\right], \tag{2a}$$

$$G_k(x, y) = \int\int_{-\infty}^{\infty} g_k(\xi, \eta) \exp\left[-\frac{i2\pi}{\lambda_k z}(x\xi + y\eta)\right] \mathrm{d}\xi\, \mathrm{d}\eta, \tag{2b}$$

for $k = \{1, \ldots, K\}$, and where z is the distance from the exit pupil to the detector. Note that the wavelength λ appears not only in $W(\xi, \eta; \lambda_k)$ due to chromatic aberrations, but also in the propagation kernel $i2\pi/(\lambda_k z)$, which effectively scales the sampling ratio (Q) according to wavelength in the discrete Fourier transform (DFT) that numerically evaluates Eq. (2b). The sampling ratio is defined as

$$Q = \frac{\lambda z}{D \Delta p}, \tag{3}$$

where D is the exit pupil diameter, and Δp is the sample spacing in the image plane [16]. The total PSF in the image plane is the incoherent sum of the spectral components:

$$I(x, y) = \sum_{k=1}^{K} |G_k(x, y)|^2. \tag{4}$$

For this study, we chose the error metric for optimization to be the normalized sum-squared difference between a simulated PSF I_s and the measured data PSF I_d:

$$E = \frac{\sum_{i,j} \left\{\left[\alpha I_s(x_i, y_j) + \beta\right] - I_d(x_i, y_j)\right\}^2}{\sum_{i,j} I_d(x_i, y_j)^2}, \tag{5}$$

where i and j index the elements of the arrays that represent I_s and I_d, and α and β are the optimal bias and gain for the given I_s and I_d, respectively [17].

In addition to the physical model, a corresponding gradient calculation is a key component of the phase retrieval process. Nonlinear optimization algorithms typically rely on the gradient of the error metric to guide their progress in a direction that minimizes it [4,18], and an analytic calculation of the gradient is much more efficient than a finite-differences technique based only on knowledge of the forward model. For this work, we utilize reverse-mode algorithmic differentiation [19,20], which is advantageous in that previous calculations for the portions of the model that are common to other problems may be reused and combined with the gradient of the unique portion of the model [20–22], which in this case is Eq. (1). Using the notation

of [19], in which the partial derivative of the final error metric E with respect to a given parameter value x is written as

$$\bar{x} \equiv \frac{\partial E}{\partial x}, \tag{6}$$

the derivatives with respect to the optimization variables in Eq. (1) are given by

$$\bar{c}_n = \sum_{i,j,k} Z_n(\xi_i, \eta_j)\overline{W}_C(\xi_i, \eta_j; \lambda_k), \tag{7a}$$

$$\overline{W}_C(\xi_i, \eta_j; \lambda_k) = \overline{W}(\xi_i, \eta_j; \lambda_k)(\lambda_k - \lambda_r), \tag{7b}$$

$$\bar{c}_n = \sum_{i,j,k} Z_n(\xi_i, \eta_j)\overline{W}(\xi_i, \eta_j; \lambda_k)(\lambda_k - \lambda_r), \tag{7c}$$

and

$$\bar{a}_n = \sum_{i,j,k} Z_n(\xi_i, \eta_j)\overline{W}_M(\xi_i, \eta_j; \lambda_k), \tag{8a}$$

$$\overline{W}_M(\xi_i, \eta_j; \lambda_k) = \overline{W}(\xi_i, \eta_j; \lambda_k), \tag{8b}$$

$$\bar{a}_n = \sum_{i,j,k} Z_n(\xi_i, \eta_j)\overline{W}(\xi_i, \eta_j; \lambda_k), \tag{8c}$$

where i and j index the elements of the arrays that represent Z_n, and $\overline{W}$, $\overline{W}_C$, and $\overline{W}_M$ are the partial derivatives of the error metric with respect to W, W_C, and W_M, respectively. The derivation for $\overline{W}$ is analogous to the example shown in [20].

B. Efficient Polychromatic Field Propagation

The simulation of polychromatic field propagation in this application presents a challenge in terms of computational efficiency. For many broadband systems, Fraunhofer propagation of electric fields can be simulated with a spatial sample spacing that is consistent across the spectrum by appropriately zero-padding the fast Fourier transform (FFT) input arrays for each spectral component. The amount of padding required is dependent on the chosen wavelengths [23]:

$$M_k = \frac{\lambda_k}{\lambda_r} M_r. \tag{9}$$

Here M_k is the array size of the kth spectral component, and M_r is the array size of the reference spectral component. However, this relationship is problematic for simulation of a narrow spectrum with many wavelength components since the incremental changes to λ_k/λ_r may be quite small, which requires that M_r be large enough to ensure that each array size M_k be an integer, giving

$$\Delta M \geq 1 \Rightarrow M_r \geq \frac{\lambda_r}{\Delta\lambda}, \tag{10}$$

where $\Delta M = M_k - M_{k-1}$, and $\Delta\lambda = \lambda_k - \lambda_{k-1}$. This requirement can increase memory usage and overall run time, and forces the choice of sample density in the pupil to be dependent on the desired spectral sample density, which is inconvenient especially when fitting a model to intensity data that are available in both pupil and image planes. In this case, it is worth considering other DFT algorithms that can simulate propagation over a finely sampled spectrum without the array size restrictions of the FFT, such as the matrix triple product (MTP) [24,25] or chirp z transform (CZT) [26,27], as demonstrated in [28]. The real-world performance of these algorithms depends on a variety of factors, such as the array size, sample densities (of the pupil and image planes as well as the spectrum), and the particular computer hardware on which the code runs. Therefore, our approach is to automatically benchmark implementations of the FFT, MTP, and CZT for a given simulation model before beginning phase retrieval and choose whichever is fastest. Because the results of these algorithms are all mathematically equivalent (except in cases where the FFT would require a non-integer pad size to be accurate), the results are consistent to within the limits of floating-point precision. We note that the floating-point roundoff error may accumulate differently depending on the algorithm, but consider this effect to be negligibly small for our application.

3. LOCAL MINIMA

In nonlinear optimization, it is possible that local minima in the error metric surface can cause the optimizer to stagnate at an incorrect solution [4], where every nearby estimate has a larger error metric. In this section, we show that the introduction of chromatic variables in phase retrieval also introduces some local minima, and determine how they may be avoided. As a simple test case, we simulated PSFs with 1.2 waves peak-to-valley (PV) of tip/tilt and one wave of defocus across an 8 nm bandwidth (or equivalently stated as 0.15 waves/nm and 0.125 waves/nm, respectively), where the PV magnitude W_{PV} of a chromatic aberration W_C over a bandwidth $B = (\lambda_K - \lambda_1)$ is defined as

$$W_{PV} = B\left\{\max\left[W_C(\xi, \eta)\right] - \min\left[W_C(\xi, \eta)\right]\right\}, \tag{11}$$

with the maximum and minimum operations being limited to the nonzero region of a hard-edged circular aperture. The angular dispersion magnitude is

$$W_C^{(1,2)}(\xi, \eta) = c_1 Z_1(\xi, \eta) + c_2 Z_2(\xi, \eta), \tag{12a}$$

$$W_{PV}^{(1,2)} = B\left\{\max\left[W_C^{(1,2)}(\xi, \eta)\right] - \min\left[W_C^{(1,2)}(\xi, \eta)\right]\right\}, \tag{12b}$$

and the axial dispersion magnitude is

$$W_C^{(4)}(\xi, \eta) = c_4 Z_4(\xi, \eta), \tag{13a}$$

$$W_{PV}^{(4)} = B\left\{\max\left[W_C^{(4)}(\xi, \eta)\right] - \min\left[W_C^{(4)}(\xi, \eta)\right]\right\}, \tag{13b}$$

where Z_1, Z_2, and Z_4 correspond with tip, tilt, and defocus, respectively. The PSFs are shown in Fig. 1, both with and without the addition of 1.5 waves of monochromatic defocus. The error metric was then evaluated for a set of PSFs with a range of values for the angular and axial dispersion as defined in Eqs. (12) and (13), and plotted the resulting 2D slice through parameter space [29] in Fig. 2. The global minimum is in the center of the

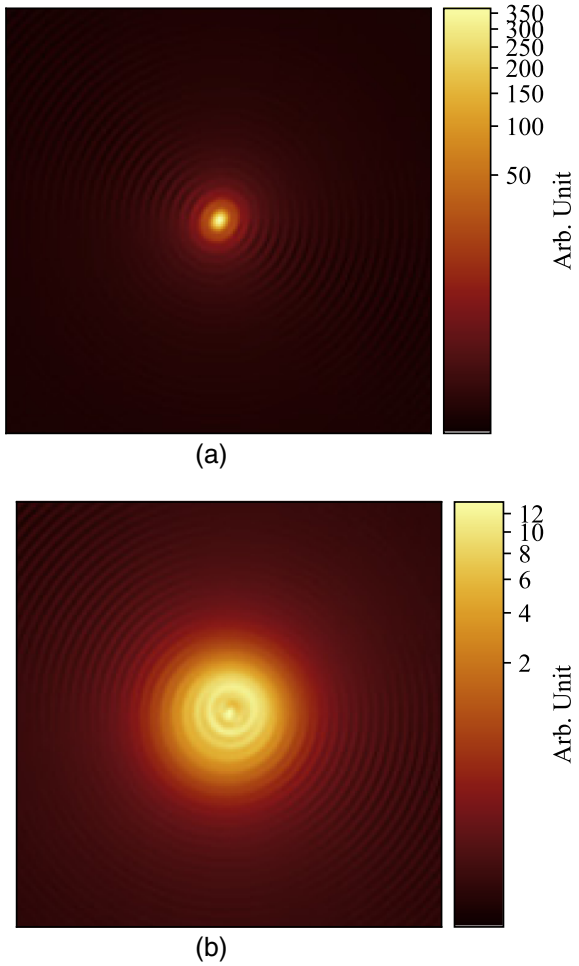

Fig. 1. PSF with axial and angular dispersion (a) in-focus and (b) 1.5 waves PV out of focus. Both are shown raised to the 0.25 power.

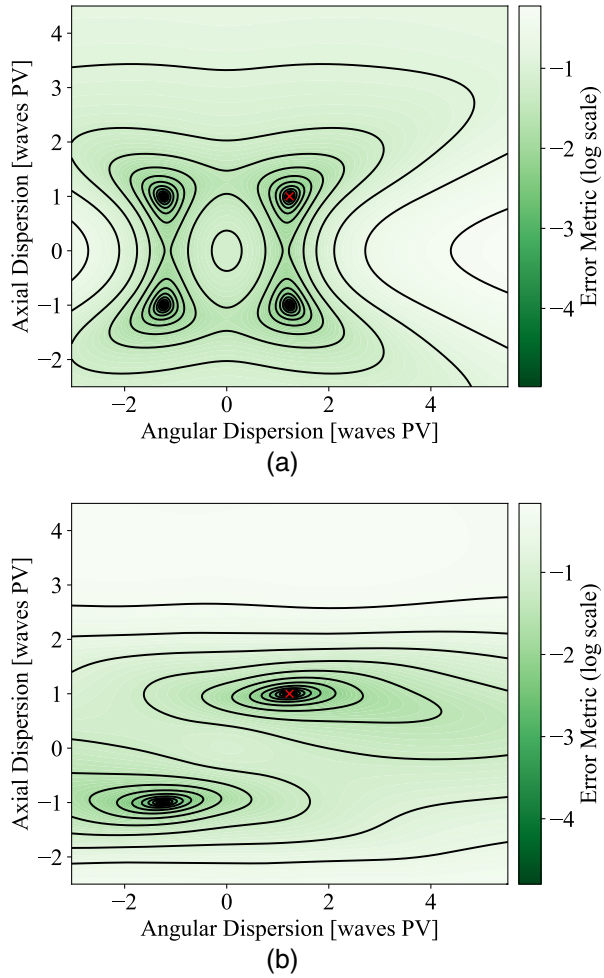

Fig. 2. Error metric as a function of the two dispersion variables, with the global minimum (correct values) in the center of the plot at coordinates (1.2, 1). The contour lines mark error metric values separated by 0.3 (on a logarithmic scale). (a) Two local minima that are present in the in-focus case (b) disappear when known defocus is added.

plot, corresponding to the true values (and zero error). Besides the global minimum in Fig. 2(a), there are also three local minima that appear where one or both of the signs of the dispersion parameters are reversed. However, when the additional known defocus is included, as in Fig. 2(b), two of the local minima disappear from the error surface.

We can explain the appearance of these minima and their relation with defocus by analogy to the well-known twin image problem in monochromatic phase retrieval [30–32]. The root cause is that the absolute value of the Fourier transform of any complex signal $f(u)$ is the same as that of its complex conjugate flipped about the origin $f^*(-u)$, which means that the twin phase in the pupil produces a simulated PSF identical to the measured one, creating an ambiguity. This is given in the 1D case as

$$\mathcal{F}\{f(u)\} \equiv \int_{-\infty}^{\infty} f(u) \exp\left[-i2\pi uv\right] \mathrm{d}u, \tag{14a}$$

$$|\mathcal{F}\{f(u)\}| = |\mathcal{F}\{f^*(-u)\}|, \tag{14b}$$

where we note that in two dimensions, reversing both coordinate axes is equivalent to a 180° rotation about the origin. Similarly, we find that if the sign of axial dispersion is reversed, the defocus element of each spectral component reverses sign and becomes that of its twin. Consider the case of a field of a spectral component $\lambda = \lambda_r + \delta\lambda$ having the amplitude weight $A(\delta\lambda)$, angular dispersion c_1, and axial dispersion c_4:

$$g(\xi;\, \delta\lambda) = A(\delta\lambda) \exp\left[i\frac{2\pi}{\lambda}\left(\delta\lambda c_1 \xi + \delta\lambda c_4 \xi^2\right)\right]. \tag{15}$$

The field corresponding to the twin phase is then

$$g^*(-\xi;\, \delta\lambda) = A(\delta\lambda) \exp\left\{-i\frac{2\pi}{\lambda}\left[\delta\lambda c_1(-\xi) + \delta\lambda c_4(-\xi)^2\right]\right\} \tag{16}$$

$$= A(\delta\lambda) \exp\left\{i\frac{2\pi}{\lambda}\left[\delta\lambda c_1 \xi + \delta\lambda(-c_4)\xi^2\right]\right\}, \tag{17}$$

thereby showing that formation of the twin is equivalent to reversal of the sign of the axial dispersion while keeping the sign of the angular dispersion, i.e.,

$$g^*(-\xi;\,\delta\lambda,\,c_4) = g(\xi;\,\delta\lambda,\,-c_4), \tag{18a}$$

$$|\mathcal{F}\{g(\xi;\,\delta\lambda,\,-c_4\}| = |\mathcal{F}\{g(\xi;\,\delta\lambda,\,c_4\}|. \tag{18b}$$

It has also been observed, in studies of monochromatic phase retrieval, that enforcing a known sign of the defocus term prevents an optimization from forming the twin phase as its estimate because the twin requires reversing the sign of every Zernike term with even radial symmetry (the components with odd radial symmetry are the same in the twin as for the true wavefront). In this case with chromatic aberrations, we can add a known defocus a_4 to the wavefront [Eq. (19)],

$$g(\xi;\,\delta\lambda, c_1,\,c_4,\,a_4) = A(\delta\lambda)\exp\left[i\frac{2\pi}{\lambda}\left(\delta\lambda c_1\xi + \delta\lambda c_4\xi^2 + a_4\xi^2\right)\right], \tag{19}$$

and observe that flipping the sign of c_4 is not sufficient to form the twin while a_4 is fixed [Eq. (20)]:

$$g(\xi;\,\delta\lambda,\,c_1,\,-c_4,\,a_4) = A(\delta\lambda)\exp\left\{i\frac{2\pi}{\lambda}\left[\delta\lambda c_1\xi + \delta\lambda(-c_4)\xi^2 + a_4\xi^2\right]\right\} \tag{20a}$$

$$= A(\delta\lambda)\exp\left\{-i\frac{2\pi}{\lambda}\left[\delta\lambda c_1(-\xi) + \delta\lambda c_4(-\xi)^2 - a_4(-\xi)^2\right]\right\} \tag{20b}$$

$$= g^*(-\xi;\,\delta\lambda,\,c_1,\,c_4,\,-a_4) \tag{20c}$$

$$\neq g^*(-\xi;\,\delta\lambda,\,c_1,\,c_4,\,a_4). \tag{20d}$$

This effect can be visualized with the ray trace in Fig. 3, which shows axial dispersion causing each spectral component to focus at a different horizontal position, and angular dispersion causing the focal points to spread vertically. The opposite sign of axial dispersion between the truth and twin images means that the blue rays, for example, cross in front of the nominal focal plane for the truth, but behind the focal plane for the twin. The red rays, representing the other end of the spectrum, do the opposite, and the green rays at the reference wavelength are unchanged. In the focal plane, both the true geometric PSF and the twin image are the same. At the defocus plane, the true PSF has one end of the spectrum further out of focus than the other, but the twin image is clearly flipped. So, the known defocus has removed the ambiguity in the sign of the axial dispersion.

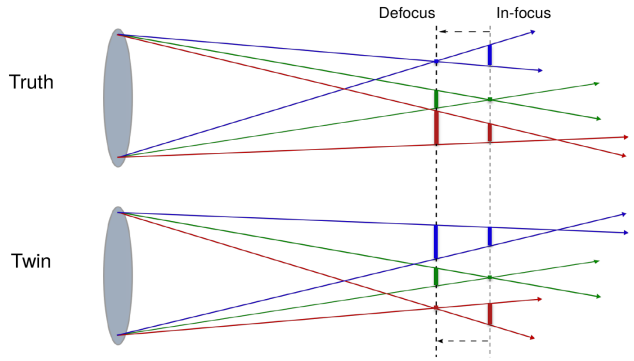

Fig. 3. Defocus eliminates the axial dispersion twin.

A somewhat similar effect is found when we try flipping the sign of angular dispersion. Without known defocus, we have, in the focal plane [Eq. (21)],

$$g(\xi;\,\delta\lambda,\,-c_1,\,c_4) = A(\delta\lambda)\exp\left\{i\frac{2\pi}{\lambda}\left[\delta\lambda(-c_1)\xi + \delta\lambda c_4\xi^2\right]\right\} \tag{21a}$$

$$= A(\delta\lambda)\exp\left\{-i\frac{2\pi}{\lambda}\left[(-\delta\lambda)c_1(-\xi) + (-\delta\lambda)c_4(-\xi)^2\right]\right\} \tag{21b}$$

$$= \frac{A(\delta\lambda)}{A(-\delta\lambda)}g^*(-\xi,\,-\delta\lambda,\,c_1,\,c_4). \tag{21c}$$

That is, reversing the sign of angular dispersion produces the twin phase of the field at the opposite end of the spectrum, $g(\xi,\,-\delta\lambda)$; however, the magnitudes of fields differ if the spectral weights are not equal. Furthermore, propagating the same wavefront at two different wavelengths does not produce the same PSF due to the scaling of diffraction effects with wavelength (i.e., the appearance of $2\pi/\lambda$ in the complex exponential). The degree to which they are similar depends on the difference in wavelength, so, if the bandwidth of a polychromatic simulation is small, the effect will be subtle. In mathematical terms,

$$|\mathcal{F}\{g(\xi;\,\delta\lambda,\,-c_1,\,c_4)\}| = \frac{A(\delta\lambda)}{A(-\delta\lambda)}|\mathcal{F}\{g^*(-\xi,\,-\delta\lambda,\,c_1,\,c_4)\}|, \tag{22a}$$

$$|\mathcal{F}\{g(\xi;\,\delta\lambda,\,-c_1,\,c_4)\}| \approx |\mathcal{F}\{g(\xi;\,-\delta\lambda,\,c_1,\,c_4)\}|. \tag{22b}$$

Therefore, whether or not the twin presents a true ambiguity, or merely a strong local minima, depends on the shape of the spectrum. If it is asymmetric such that $A(\delta\lambda) \neq A(-\delta\lambda)$ and is not too narrow, then the true PSF and twin image may be different enough that the error metric at the twin will be significantly larger than the error metric at the true solution. If defocus is added, we find

$$g(\xi;\, \delta\lambda,\, -c_1,\, c_4,\, a_4) = A(\delta\lambda)\exp\left\{i\frac{2\pi}{\lambda}\left[\delta\lambda(-c_1)\xi + \delta\lambda c_4\xi^2 + a_4\xi^2\right]\right\} \tag{23a}$$

$$= A(\delta\lambda)\exp\left[-i\frac{2\pi}{\lambda}\left(\delta\lambda c_1\xi - \delta\lambda c_4\xi^2 - a_4\xi^2\right)\right] \tag{23b}$$

$$= A(\delta\lambda)\exp\left\{-i\frac{2\pi}{\lambda}[(-\delta\lambda)c_1(-\xi) + (-\delta\lambda)c_4(-\xi)^2 - a_4(-\xi)^2]\right\} \tag{23c}$$

$$= \frac{A(\delta\lambda)}{A(-\delta\lambda)}g^*(-\xi;\, -\delta\lambda,\, c_1,\, c_4,\, -a_4) \tag{23d}$$

$$\neq \frac{A(\delta\lambda)}{A(-\delta\lambda)}g^*(-\xi;\, -\delta\lambda,\, c_1,\, c_4,\, a_4). \tag{23e}$$

So, known defocus also removes the ambiguity in the sign of angular dispersion, as it did for axial. This is also illustrated by the ray trace in Fig. 4, where the difference between the truth and twin is the direction of angular dispersion. In the focal plane, they are similar, but the spectral components are out of order. In the defocus plane, the truth and twin are clearly opposites.

Finally, we consider the third local minima that appeared in the error metric surface of Fig. 2(a) and persisted in Fig. 2(b), where the signs of angular and axial dispersion are simultaneously reversed. In this case,

$$g(\xi;\, \delta\lambda,\, -c_1,\, -c_4,\, a_4) = A(\delta\lambda)\exp\left\{i\frac{2\pi}{\lambda}\left[\delta\lambda(-c_1)\xi + \delta\lambda(-c_4)\xi^2 + a_4\xi^2\right]\right\} \tag{24a}$$

$$= A(\delta\lambda)\exp\left\{i\frac{2\pi}{\lambda}\left[(-\delta\lambda)c_1\xi + (-\delta\lambda)c_4\xi^2 + a_4\xi^2\right]\right\} \tag{24b}$$

$$= \frac{A(\delta\lambda)}{A(-\delta\lambda)}g(\xi;\, -\delta\lambda,\, c_1,\, c_4,\, a_4). \tag{24c}$$

$$|\mathcal{F}\{g(\xi;\, \delta\lambda,\, -c_1,\, -c_4,\, a_4)\}| = \frac{A(\delta\lambda)}{A(-\delta\lambda)}|\mathcal{F}\{g(\xi;\, -\delta\lambda,\, c_1,\, c_4,\, a_4)\}|. \tag{25}$$

Now, we see that each spectral component $\delta\lambda$ has taken on the wavefront of its counterpart on the opposite side of the spectrum, $-\delta\lambda$. However, similar to the case where angular dispersion was reversed alone, the PSF produced is different due to the scaling effect of the wavenumber $2\pi/\lambda$ in the complex exponential and any asymmetry in the spectrum. In contrast to the previous cases, a known defocus does not resolve the ambiguity because these are not twin images. Instead, the individual spectral components have swapped places in the image plane. This is also illustrated in Fig. 5, where we see that in both planes the size and location of individual monochromatic PSFs are correct except for having the wrong wavelength.

In summary, the two minima that occur when a single dispersion term is flipped are removed if a known defocus is enforced, because the twin phase at each spectral component would require the reference defocus to also be flipped. The local minimum that still remains in Fig. 2(b) sits where the dispersion coefficients are reversed together, which is equivalent to reversing the sign of the $\delta\lambda$; however, this is not a true ambiguity due to the wavelength dependence of diffraction and possibly asymmetry in the spectrum. These effects are subtle over a small bandwidth such as the 8 nm in pulses from OMEGA EP, but may produce a significantly higher error metric than the true solution. If so, then a sufficient strategy for avoiding this minimum is to check the error metric against a threshold value after the optimizer converges, and if it is too high, reverse the signs of the dispersion coefficients and perform another round of local nonlinear optimization.

4. MONTE CARLO SIMULATION

To test the strategy presented in Section 3, the algorithm was run through a series of trials with a variety of simulated true reference wavefronts and various starting guesses for the dispersion parameters. In all cases, the true chromatic aberrations were 1.2 waves PV of angular dispersion and one wave PV of axial dispersion across an 8 nm bandwidth (or equivalently stated as 0.15 waves/nm and 0.125 waves/nm, respectively), which are comparable to previously estimated values for OMEGA

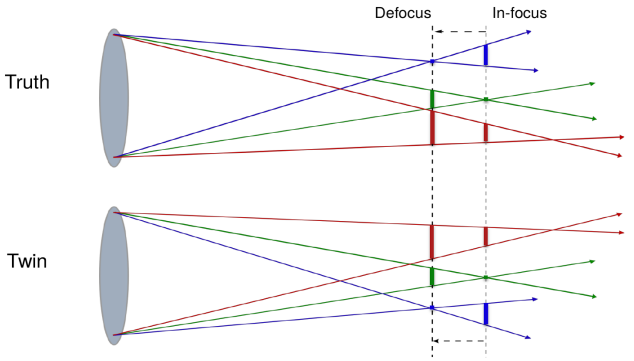

Fig. 4. Defocus eliminates the angular dispersion twin.

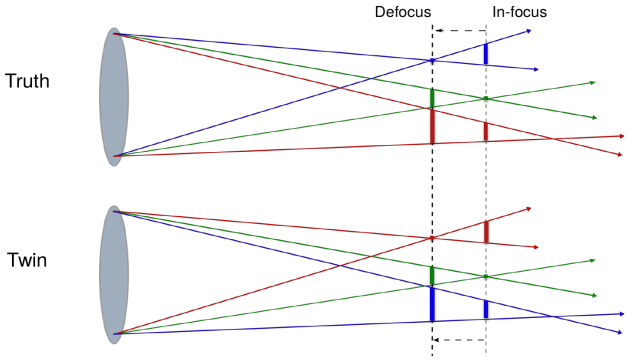

Fig. 5. Defocus does not eliminate the joint axial-angular twin.

EP [8]. The spectral weights for intensity given as the square of the spectral weights for amplitude, $S(\lambda) = A^2(\lambda)$, are shown in Fig. 6. This is representative of measured spectra in fully amplified shots of OMEGA EP, which follow from the spectral gain of the Nd-doped phosphate glass amplifiers in the main beamline. The randomized true reference wavefronts were each the sum of a known part W_0 (simulating data from a SHWFS) with a magnitude 0.4 waves rms and an unknown part W_M (simulating non-common path error) that had to be retrieved and had a magnitude of 0.11 waves rms. Defocus in the amount of 1.5 waves was also added, and assumed to be known. In each case, the true PSF had a peak value of 72×10^3 photons, and shot noise was included as well as seven electrons rms Gaussian read noise after applying an assumed 80% quantum efficiency. The trial cases included five independent random realizations of W_0, five independent random realizations of W_M, and 64 initial estimates for the dispersion parameters. These three sets of parameters were combined to make a total of $(5 \times 5 \times 64) = 1600$ trials. The initial estimates for the dispersion parameters were selected from a uniform distribution of parameter values ranging between a factor of -2 and $+2$ times the true values. The random Zernike coefficients used to simulate W_0 were drawn from a power law distribution that mimics atmospheric turbulence, and the coefficients of the non-common path wavefront were generated using statistics based on previous calibrations of non-common path error in OMEGA EP diagnostics [8]. A representative wavefront at the central wavelength and polychromatic PSF including dispersion are shown in Fig. 7.

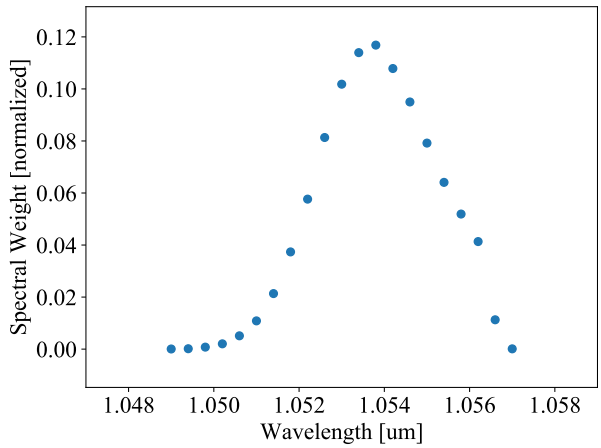

Fig. 6. Intensity spectrum ($S = A^2$) used in Monte Carlo simulations.

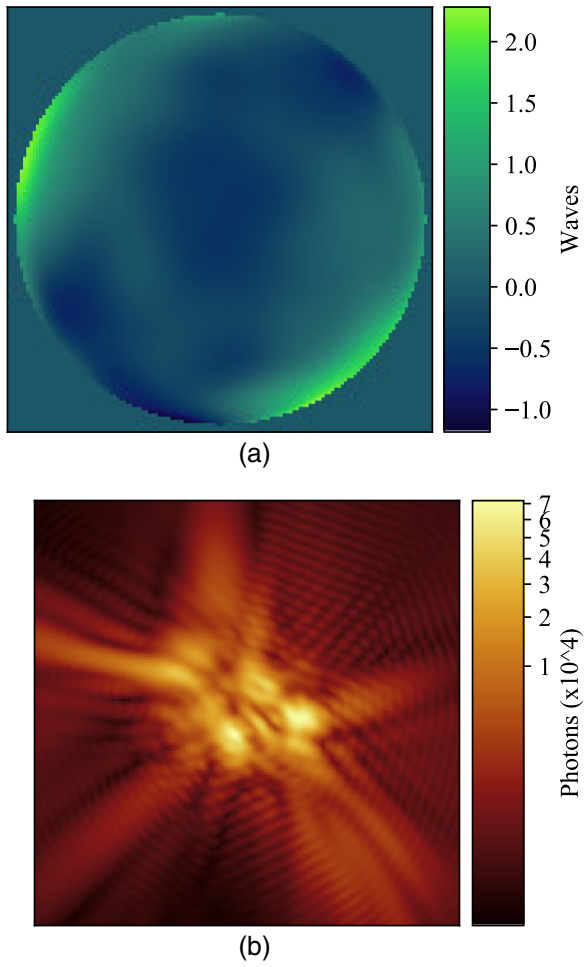

Fig. 7. Representative example of random simulated data. (a) Wavefront aberration (defocus removed for visualization) and (b) PSF (0.25 power stretch).

Both the unknown part of the monochromatic reference wavefront and the dispersion terms were retrieved, but it was found that a good solution was more likely to be obtained if the optimization proceeded in two stages. In the first stage, the

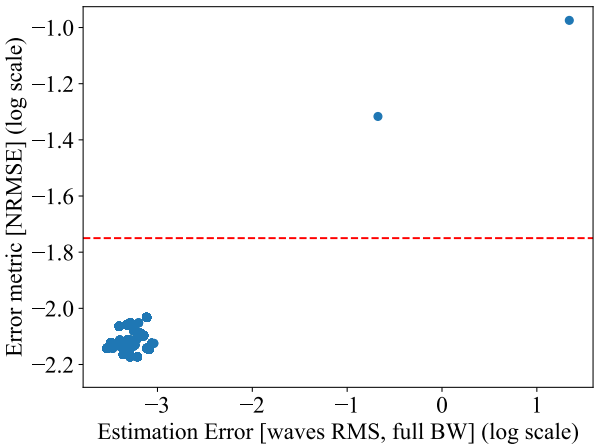

Fig. 8. Phase-retrieval error metric versus error of the reconstruction, where the error is computed over the full bandwidth. Successful cases have low estimation error, and failed cases are identifiable by a large error metric in the PSF fit. In this example, cases above the red dashed line are considered failed cases, and the ones below the line are considered successful.

monochromatic reference wavefront was optimized alone while the dispersion terms were left at zero. Once that converged, a second stage was carried out by first choosing a random initial estimate for the dispersion, and then allowing both the monochromatic and dispersion terms to vary in a second round of optimization. This progression in stages is analogous to bootstrapping methods that have proved successful in other phase-retrieval applications [32,33]. In combination with the twin phase check described at the end of Section 3, this strategy was successful in all but two of the 1600 tested cases. For the successful cases, the estimated wavefronts came within one thousandth of a wave rms of the true solution, where the mean difference within the rms is computed over all spectral components. In the failed cases, the normalized root-mean-squared error (NRMSE), the square root of Eq. (5), between the estimated and true PSFs was in the neighborhood of 10 times greater than the error metric for successful cases, as shown by the outliers in Fig. 8. Therefore, if one of these failures occurs in practice, it can be recognized by the large residual error metric and recovered from by performing another optimization run from a different random starting point.

5. LABORATORY EXPERIMENT

To test the proposed chromatic aberration retrieval algorithm in a real-world scenario, we also applied the method to a small-scale laboratory test setup. This test bed was previously built to generate and measure chromatic aberrations with a method that utilizes a 2D grating to simultaneously disperse spectral components and provide focus diversity [34,35]. In this section, we seek to reproduce that measurement with the approach discussed in this paper. For consistency with [34], we will represent angular and axial dispersion in terms of pulse front delay (PFD) and radial group delay (RGD), respectively, which for an optical field $u(x, y, \Omega)$ are defined as β and γ such that

$$u(x, y, \Omega) = a_0(x, y) A(\Omega) \exp[i\phi_0(x, y)] \times \exp\left\{ i\Omega \left[\beta_x \frac{x}{r_0} + \beta_y \frac{y}{r_0} + \gamma \left(\frac{r}{r_0} \right)^2 \right] \right\}, \tag{26}$$

where $a_0(x, y)$ is the amplitude, $A(\Omega)$ is the spectral weight, $\phi_0(x, y)$ is the phase at the reference wavelength, r_0 is the nominal beam radius, and $\Omega \equiv \omega - \omega_0$ is defined as the difference in angular frequency between a given spectral component and the reference.

A. Equipment and Methodology

The conceptual layout of the experimental setup is shown in Fig. 9. A Superlum SLD-52 super-luminescent light-emitting diode (SLED) served as a broadband light source, having a bandwidth of approximately 100 nm and spectral distribution of intensity, where $S(\lambda) = A^2(\lambda)$, shown in Fig. 10. The output of the SLED was fiber coupled, and collimated with a

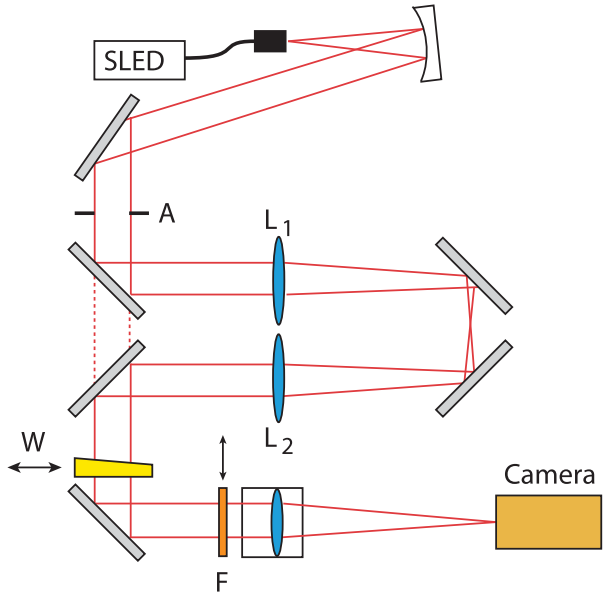

Fig. 9. Experimental system layout. Reprinted from [34].

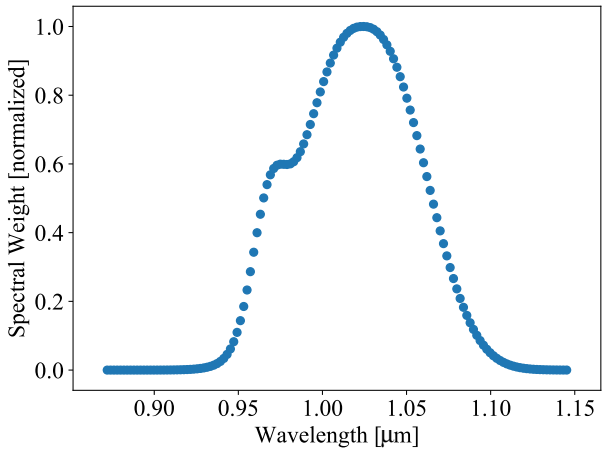

Fig. 10. Intensity spectrum of the SLED.

concave mirror before being passed through a square apodizer (A) that had a 2D super-Gaussian profile and a full-width at half-maximum (FWHM) for intensity at 7 mm. Therefore, the value for the normalized beam radius used in Eq. (26) will be $r_0 = 3.5$ mm. Given the large bandwidth of the source, significant chromatic dispersion can be introduced with a few glass elements. To that end, the beam was relayed through a pair of 103 mm plano–convex fused-silica lenses (L1 and L2), which together provided $\gamma = 10.0$ fs of RGD. A fused-silica wedge (W) with 1° apex angle imparted $\beta = 2.5$ fs of PFD (or equivalently $2\beta = 5$ fs PV PFD as recorded in [34]). For some tests, a Semrock LL01-1030-12.5 narrowband filter (F) with a FWHM bandwidth of less than 7.2 nm and central wavelength of 1.03 μm was inserted to provide images that are effectively monochromatic (the chromatic aberrations are negligible over this range) and can serve as a reference. The beam was focused with a 200 mm achromatic doublet, and images of the PSF were captured by a JAI Pulnix TM-4200 GE monochrome charge-coupled device (CCD) camera, which has a pixel pitch of 7.4 μm. For phase retrieval, the camera was translated along the optical axis to provide focus diversity. The focus sweep was performed first with the spectral filter, then again with it replaced by a neutral density (ND) filter. For each image, the exposure time was adjusted so that roughly 80% of the well depth was filled at the brightest spot in the image. Because the broadband illumination had much greater total energy than the monochromatic beam, a ND filter with optical density (OD) 2.0 was used when the spectral filter was absent to prevent saturating the detector. The nominal sampling ratio at the focal plane was $Q = [(1.03\ \mu\text{m})(200\ \text{mm})]/[(7.0\ \text{mm})(7.4\ \mu\text{m})] = 4.0$, which is twice the Nyquist limit for intensities and is expected to be more than adequate. It should be noted that Q is dependent on wavelength and so varies across the spectrum, and because the system is not telecentric it depends on the detector shift as well. Since the focus position was only roughly measured in these tests, the nominal Q value was used merely as a starting point for later optimization [21]. Images of the pupil amplitude distribution were also obtained by removing the focusing lens and observing the collimated beam.

1. Monochromatic

The set of data analyzed in this section was taken with the narrowband spectral filter in place, to provide images with no chromatic aberration. From these, we can measure the monochromatic contribution to the wavefront without the risk of confounding effects from dispersion. The beam intensity distribution due to the apodizer (marked as A in Fig. 9) was measured by removing the focusing lens, and the square root of the data was taken to produce the amplitude shown in Fig. 11(a). The detector is not in a conjugate plane to the pupil for this measurement, so some near-field diffraction effects are to be expected. To compensate for this as well as to filter noise, the measured amplitude was fit to a 2D super-Gaussian distribution as shown in Fig. 11(b) for use in the starting point for phase retrieval. A 1D horizontal slice through the center of the pupil image and its super-Gaussian fit are shown in Fig. 12, where we see that the pupil image data have bumps at the base of the

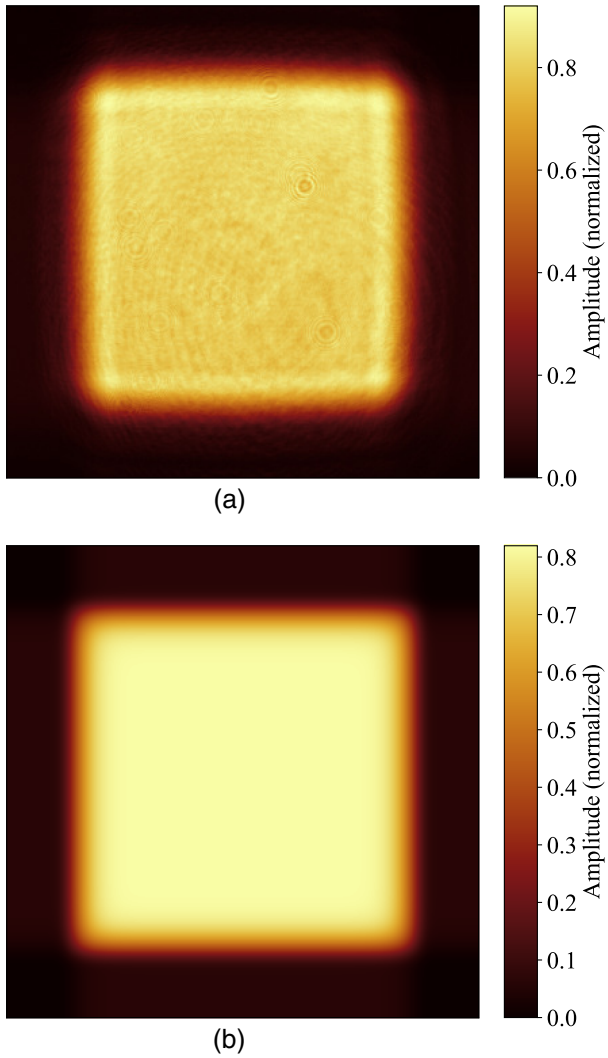

Fig. 11. Pupil amplitude. (a) Measured and (b) super-Gaussian fit.

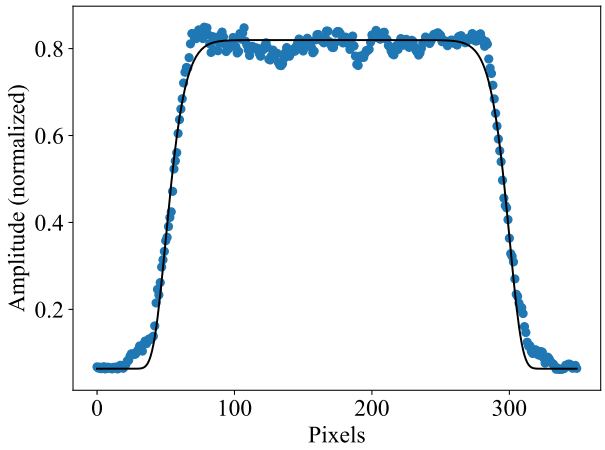

Fig. 12. Pupil amplitude cut through. The circles mark measured data points, and the solid line is the super-Gaussian fit.

curve that are likely the effect of near-field diffraction. The raw PSF images were used without modification, and are shown in Fig. 13. To account for overall signal bias and gain in the PSF

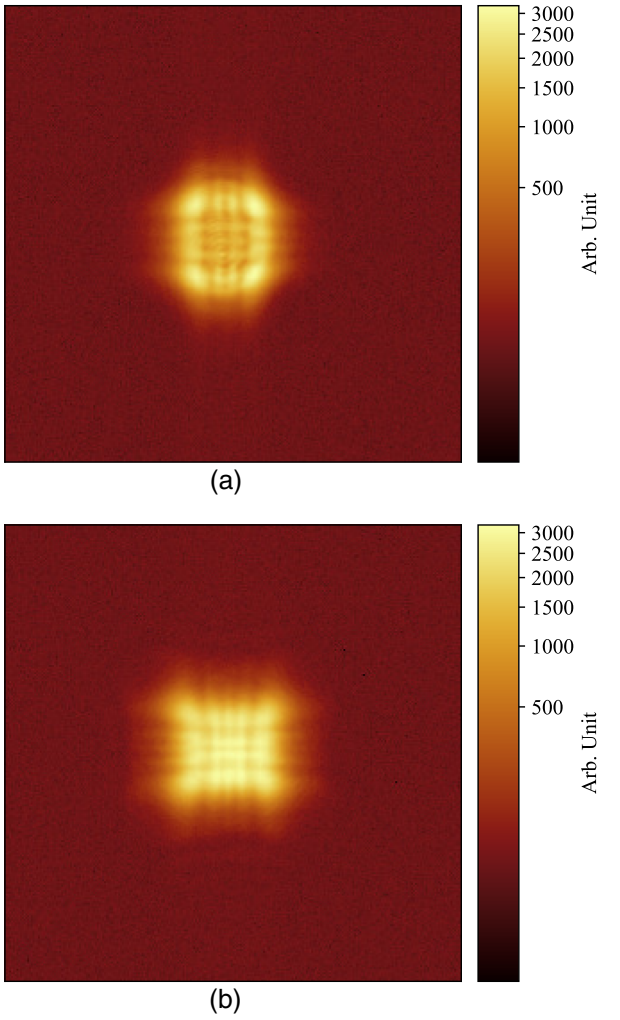

Fig. 13. Measured PSFs with monochromatic filter. (a) Before focus and (b) after focus.

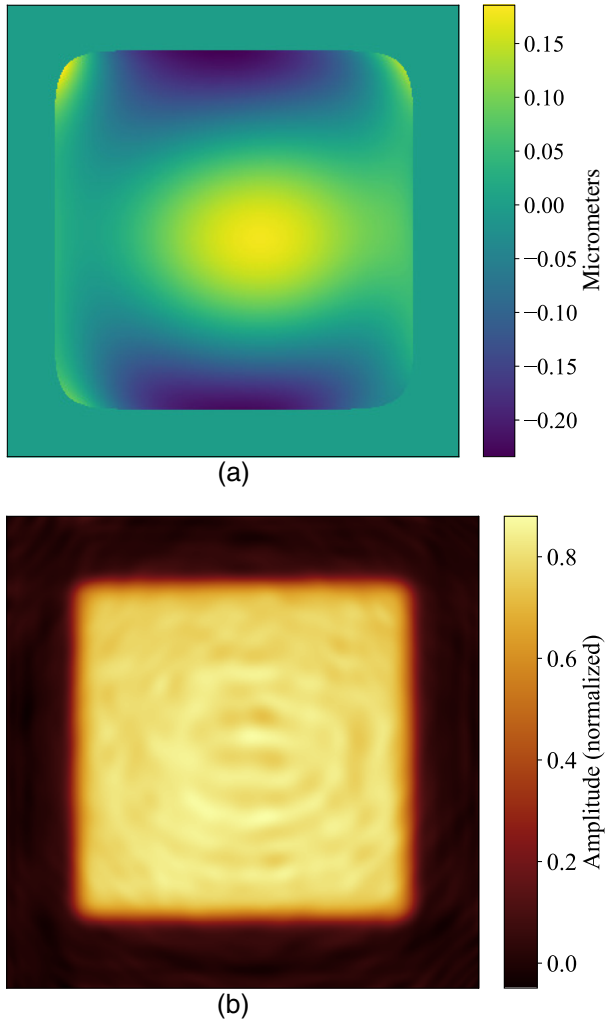

Fig. 14. Final pupil estimate (monochromatic). (a) Wavefront and (b) amplitude.

images, a bias and gain insensitive error metric was used for the phase retrieval [17].

The fitting process was carried out in multiple stages in which a limited selection of parameters was allowed to vary. The first variables to be optimized were focus, tip, tilt, and Q, providing a low-order fit. Then, the wavefront was retrieved in terms of Zernike polynomials, followed by adjustment of the point-by-point representation of the pupil amplitude. In the final step, all variables (wavefront, Q, and amplitude) were jointly optimized.

The optimization process converged to a solution where the NRMSE value was 3.15%. The final wavefront and amplitude estimates are shown in Fig. 14, where we see that the wavefront is similar to the result in [34]. The estimated values of Q for the defocus planes before and after focus were $Q = 4.14$ and $Q = 3.81$, respectively, and the amounts of defocus were found to be -1.77 μm and 2.14 μm PV over the 7 mm nominal width of the beam.

2. Full Bandwidth

A second set of PSF images, shown in Fig. 15, was captured with the full spectrum of the SLED and exhibit a very subtle blurring effect due to dispersion and the increased bandwidth. Because these effects are small, the more-dominant aberrations were estimated before the dispersion parameters to prevent them from being pushed into a local minimum. As a first step in the process, the estimates for focus, tip/tilt, and Q previously obtained from the monochromatic data were re-optimized for the new images, resulting in minor adjustments. Some variation in these values between the monochromatic and full-bandwidth estimates is expected because the detector was moved through focus before and after when the filters were changed, and the positions were not perfectly repeated. The monochromatic wavefront was then estimated in terms of Zernike coefficients, using zeros as the starting point and a super-Gaussian best fit as the pupil amplitude. This is analogous to a situation where focus, tip, tilt, and Q are constant and well-known system parameters, but the wavefront and amplitude are variable (e.g., due to atmospheric turbulence and thermal variations), and monochromatic images are not available. For dispersion retrieval, eight discrete spectral samples were selected for inclusion in the model (Fig. 16), and the dispersion was parameterized in terms of coefficients that vary tip, tilt, and focus linearly with wavelength. Last, all of the

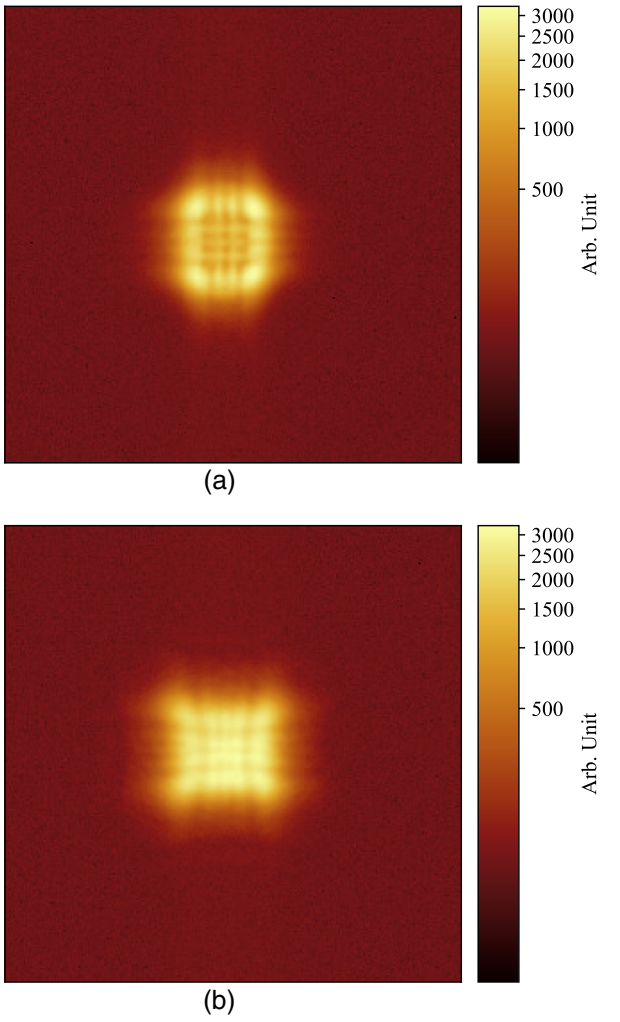

Fig. 15. Measured PSFs (full bandwidth). (a) Before focus and (b) after focus.

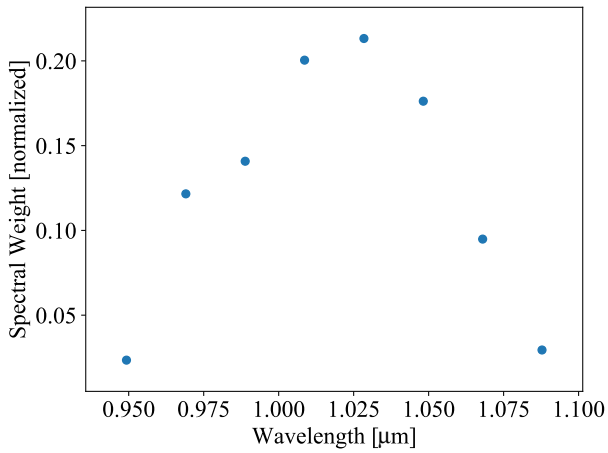

Fig. 16. Spectral samples used for dispersion model.

variables (wavefront, amplitude, Q, and dispersion) were jointly optimized to produce the final estimate. The NRMSE between the estimated PSFs and measured data is 2.88%.

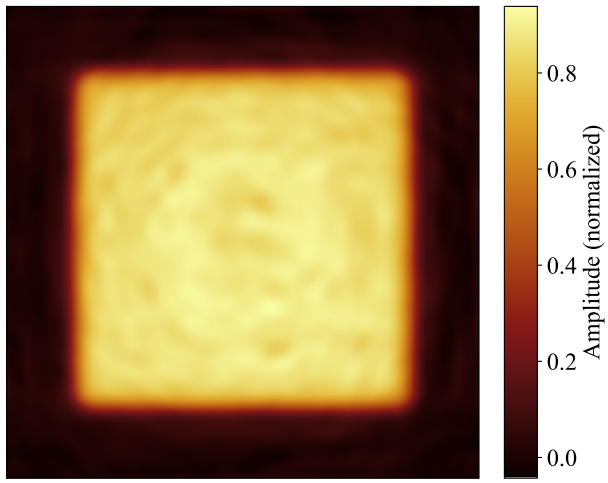

Fig. 17. Final amplitude estimate (full bandwidth).

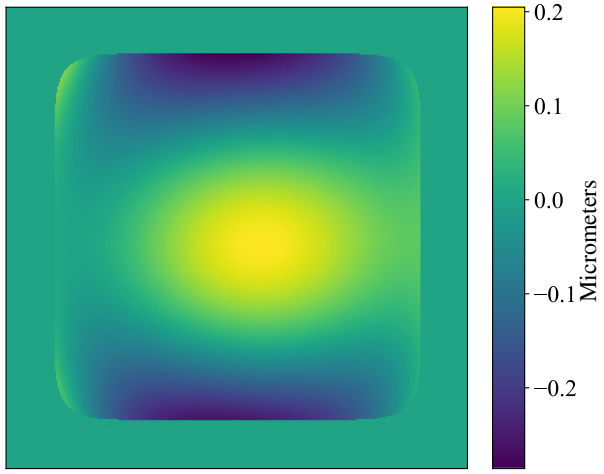

Fig. 18. Final wavefront estimate (full bandwidth).

The final pupil amplitude and wavefront estimates are shown in Fig. 17 and Fig. 18, respectively, where we see that the monochromatic wavefront is again similar to the previous result in [34]. The difference between this estimate and the one based on monochromatic data in Section 5.A.1 is only 16.9 nm rms over a 7 mm square pupil region. The Q and defocus amounts stayed near the initial values obtained from the monochromatic data, with $Q = 4.17$ and $Q = 3.83$ for before and after focus, respectively, and defocus at -1.71 μm and 2.17 μm PV. The final dispersion estimate consisted of 4.68 fs of PFD and 9.13 fs of RGD, which differ by 6.4% and 8.7% from the expected values of 5.0 fs and 10.0 fs, respectively. Compared to the results in [34], where the PFD estimate was within 0.5 fs of expectations and the RGD within 0.1 fs, these results for PFD are similar, while the RGD is less accurate. To visualize the scale of the chromatic aberrations, the difference between the wavefronts at the two ends of the spectrum (0.949 μm and 1.09 μm) is shown in Fig. 19, where we see the large change in focus due to RGD, as well as a change in the horizontal tilt due to PFD.

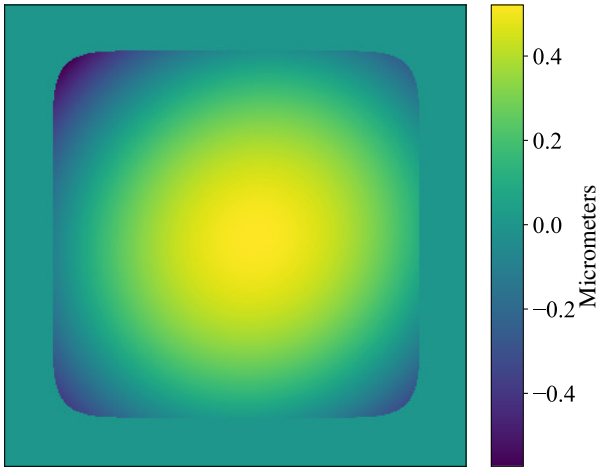

Fig. 19. Difference between the wavefront estimates at the two ends of the spectrum illustrates the range of focus and tilt due to RGD and PFD.

6. CONCLUSION

In this paper, we have developed a simulation model and optimization process for the joint estimation of linear chromatic aberrations in addition to monochromatic aberrations using a measured broadband PSF together with a known aperture, spectrum, and initial wavefront estimate. Particular attention was paid to system parameters relevant to application to the OMEGA EP laser.

To prevent ambiguities and local minima, we used a Zernike-based parameterization of the chromatic aberrations, as well as addition of known defocus to reduce sign ambiguities. A remaining local minimum that produces the incorrect sign for all chromatic aberration parameters does exist, but is not a true ambiguity and can be identified if the spectrum is asymmetric or not overly narrow. In simulation, we found a bootstrapping strategy that first estimated the monochromatic wavefront correction followed by optimization of the chromatic parameters to be highly successful.

A test of this approach in a laboratory experiment also produced encouraging results. Putting the method into practice for OMEGA EP will require improving the simulation model to more closely match the real properties of this complex system. However, the method does provide the benefit of being less susceptible to non-common path error than techniques that require additional optical elements.

Funding. National Nuclear Security Administration (DE-NA0003856); University of Rochester; New York State Energy Research and Development Authority.

Acknowledgment. Portions of this work were presented at the OSA Imaging and Applied Optics Meeting in 2013, paper OW3A.2, and in 2016, paper CT4C.5. We thank the Frank J. Horton Research Fellowship of the Laboratory for Laser Energetics for supporting this research. We also thank Alden Jurling for collaboration on core phase retrieval software tools. The support of the Department of Energy (DOE) does not constitute an endorsement by DOE of the views expressed in this paper.

Disclosures. The authors declare no conflicts of interest.

Data Availability. Data underlying the results presented in this paper are not publicly available at this time but may be obtained from the authors upon reasonable request.

REFERENCES

1. R. A. Gonsalves, "Phase retrieval from modulus data," J. Opt. Soc. Am. **66**, 961–964 (1976).
2. J. N. Cederquist, J. R. Fienup, C. C. Wackerman, S. R. Robinson, and D. Kryskowski, "Wave-front phase estimation from Fourier intensity measurements," J. Opt. Soc. Am. A **6**, 1020–1026 (1989).
3. J. R. Fienup, "Phase retrieval algorithms: a comparison," Appl. Opt. **21**, 2758–2769 (1982).
4. J. Nocedal and S. J. Wright, *Numerical Optimization* (Springer, 2006).
5. R. Fletcher, *Practical Methods of Optimization* (Wiley, 2000).
6. J. H. Kelly, L. J. Waxer, V. Bagnoud, I. A. Begishev, J. Bromage, B. E. Kruschwitz, T. J. Kessler, S. J. Loucks, D. N. Maywar, R. L. McCrory, D. D. Meyerhofer, S. F. Morse, J. B. Oliver, A. L. Rigatti, A. W. Schmid, C. Stoeckl, S. Dalton, L. Folnsbee, M. J. Guardalben, R. Jungquist, J. Puth, M. J. Shoup, D. Weiner, and J. D. Zuegel, "OMEGA EP: high-energy petawatt capability for the OMEGA laser facility," J. Phys. IV **133**, 75–80 (2006).
7. J. Bromage, S.-W. Bahk, D. Irwin, J. Kwiatkowski, A. Pruyne, M. Millecchia, M. Moore, and J. D. Zuegel, "A focal-spot diagnostic for on-shot characterization of high-energy petawatt lasers," Opt. Express **16**, 16561–16572 (2008).
8. B. E. Kruschwitz, S.-W. Bahk, J. Bromage, M. D. Moore, and D. Irwin, "Accurate target-plane focal-spot characterization in high-energy laser systems using phase retrieval," Opt. Express **20**, 20874–20883 (2012).
9. S.-W. Bahk, J. Bromage, I. A. Begishev, C. Mileham, C. Stoeckl, M. Storm, and J. D. Zuegel, "On-shot focal-spot characterization technique using phase retrieval," Appl. Opt. **47**, 4589–4597 (2008).
10. G. Pretzler, A. Kasper, and K. Witte, "Angular chirp and tilted light pulses in CPA lasers," Appl. Phys. B **70**, 1–9 (2000).
11. K. Osvay, A. Kovacs, Z. Heiner, G. Kurdi, J. Klebniczki, and M. Csatari, "Angular dispersion and temporal change of femtosecond pulses from misaligned pulse compressors," IEEE J. Sel. Top. Quantum Electron. **10**, 213–220 (2004).
12. H.-M. Heuck, P. Neumayer, T. Kühl, and U. Wittrock, "Chromatic aberration in petawatt-class lasers," Appl. Phys. B **84**, 421–428 (2006).
13. J. Bromage, S.-W. Bahk, I. A. Begishev, C. Dorrer, M. J. Guardalben, B. N. Hoffman, J. Oliver, R. G. Roides, E. M. Schiesser, M. J. Shoup, III, M. Spilatro, B. Webb, D. Weiner, and J. D. Zuegel, "Technology development for ultraintense all-OPCPA systems," High Power Laser Sci. Eng. **7**, e4 (2019).
14. W. H. Williams, J. K. Crane, D. A. Alessi, C. D. Boley, M. W. Bowers, A. D. Conder, J.-M. G. Di Nicola, P. Di Nicola, C. Haefner, J. M. Halpin, M. Y. Hamamoto, J. E. Heebner, M. R. Hermann, S. I. Herriot, D. C. Homoelle, D. H. Kalantar, T. E. Lanier, K. N. LaFortune, J. K. Lawson, R. R. Lowe-Webb, F. X. Morrissey, H. Nguyen, C. D. Orth, L. J. Pelz, M. A. Prantil, M. C. Rushford, R. A. Sacks, J. T. Salmon, L. G. Seppala, M. J. Shaw, R. J. Sigurdsson, P. J. Wegner, C. C. Widmayer, S. T. Yang, and T. L. Zobrist, "Spatio-temporal focal spot characterization and modeling of the NIF ARC kilojoule picosecond laser," Appl. Opt. **60**, 2288–2303 (2021).
15. G. R. Brady, K. Schrader, S. A. Kemme, and E. A. Shields, "Broadband phase-diverse phase retrieval in systems with chromatic aberration," in *Frontiers in Optics*, OSA Technical Digest (CD) (Optical Society of America, 2010), paper PDPA2.

16. R. D. Fiete, "Image quality and λFN/p for remote sensing systems," Opt. Eng. **38**, 1229–1240 (1999).
17. S. T. Thurman and J. R. Fienup, "Phase retrieval with signal bias," J. Opt. Soc. Am. A **26**, 1008–1014 (2009).
18. R. Fletcher, *Practical Methods of Optimization* (Wiley, 1987), Vol. **1**.
19. A. Griewank and A. Walther, *Evaluating Derivatives: Principles and Techniques of Algorithmic Differentiation* (Society for Industrial and Applied Mathematics, 2008).
20. A. S. Jurling and J. R. Fienup, "Applications of algorithmic differentiation to phase retrieval algorithms," J. Opt. Soc. Am. A **31**, 1348–1359 (2014).
21. A. S. Jurling and J. R. Fienup, "Phase retrieval with unknown sampling factors via the two-dimensional chirp z-transform," J. Opt. Soc. Am. A **31**, 1904–1911 (2014).
22. J. R. Fienup, "Phase-retrieval algorithms for a complicated optical system," Appl. Opt. **32**, 1737–1746 (1993).
23. J. R. Fienup, "Phase retrieval for undersampled broadband images," J. Opt. Soc. Am. A **16**, 1831–1837 (1999), with a corrected version of Eq. (4).
24. R. Soummer, L. Pueyo, A. Sivaramakrishnan, and R. J. Vanderbei, "Fast computation of Lyot-style coronagraph propagation," Opt. Express **15**, 15935–15951 (2007).
25. M. Guizar-Sicairos, S. T. Thurman, and J. R. Fienup, "Efficient subpixel image registration algorithms," Opt. Lett. **33**, 156–158 (2008).
26. L. Rabiner, R. Schafer, and C. Rader, "The chirp z-transform algorithm," IEEE Trans. Audio Electroacoust. **17**, 86–92 (1969).
27. L. Bluestein, "A linear filtering approach to the computation of discrete Fourier transform," IEEE Trans. Audio Electroacoust. **18**, 451–455 (1970).
28. A. S. Jurling, M. D. Bergkoetter, and J. R. Fienup, "Techniques for arbitrary sampling in two-dimensional Fourier transforms," J. Opt. Soc. Am. A **35**, 1784–1796 (2018).
29. A. S. Jurling and J. R. Fienup, "A numerical exploration of phase-retrieval error-metric surfaces," Proc. SPIE **9148**, 91486N (2014).
30. J. R. Fienup and C. C. Wackerman, "Phase-retrieval stagnation problems and solutions," J. Opt. Soc. Am. A **3**, 1897–1907 (1986).
31. M. Guizar-Sicairos and J. R. Fienup, "Understanding the twin-image problem in phase retrieval," J. Opt. Soc. Am. A **29**, 2367–2375 (2012).
32. M. D. Bergkoetter and J. R. Fienup, "Increasing capture range of phase retrieval on a large scale laser system," in *Imaging and Applied Optics* (Optical Society of America, 2015), paper CW4E.3.
33. J. R. Fienup, J. C. Marron, T. J. Schulz, and J. H. Seldin, "Hubble Space Telescope characterized by using phase-retrieval algorithms," Appl. Opt. **32**, 1747–1767 (1993).
34. S.-W. Bahk, C. Dorrer, and J. Bromage, "Two-dimensional single-shot characterization of spatiotemporal coupling of ultrashort pulses using chromatic diversity," in *Imaging and Applied Optics* (Optical Society of America, 2017), paper CW1B.5.
35. S.-W. Bahk, C. Dorrer, and J. Bromage, "Chromatic diversity: a new approach for characterizing spatiotemporal coupling of ultrashort pulses," Opt. Express **26**, 8767–8777 (2018).